Chapter 2

Optical FMCW Reflectometry

2.1 Introduction

The centerpiece and workhorse of the research described in this thesis is the optoelec-
tronic swept-frequency laser (SFL)—a feedback system designed around a frequency-
agile laser to produce precisely linear optical frequency sweeps (chirps) [1–3]. This sys-
tem is studied in detail in chapter 3. In the present chapter, by way of introduction, we
focus on an application of swept-frequency waveforms, optical frequency-modulated
continuous-wave (FMCW) reflectometry, and its use in three-dimensional (3-D) imag-
ing. We examine how chirp characteristics affect application metrics and therefore
motivate the choices made in the design of the optoelectronic SFL.

The fundamental challenge of 3-D imaging is ranging—the retrieval of depth in-
formation from a scene or a sample. One way to construct a 3-D imaging system
is to launch a laser beam along a particular axis, and collect the reflected light, in
an effort to determine the depths of all the scatterers encountered by the beam as it
propagates. A 3-D image may then be recorded by scanning the beam over the entire
object space.

A conceptually simple way to retrieve depth information is to launch optical pulses,
and record arrival times of the reflections. Scatterer depth can then be calculated
by multiplying the arrival times by the speed of light c. Implementations based on
this idea, collectively known as time-of-flight (TOF) systems, have been successfully
demonstrated [16, 17]. The depth resolution, also called range resolution or axial

resolution, of TOF methods depends on the system's ability to generate and record temporally narrow optical pulses. A state-of-the-art TOF system therefore requires a costly pulse source, e.g., a mode-locked laser, and a high-bandwidth detector [37]. A detection bandwidth of 1 GHz yields a resolution of $\Delta z \propto c \times (1 \text{ ns}) = 30$ cm in free space. Improvement of the resolution to the sub-mm range requires detectors with 100s of GHz of bandwidth, and is prohibitively expensive with current technology.

The technique of frequency-modulated continuous-wave (FMCW) reflectometry, originally developed for radio detection and ranging (radar), can be applied to the optical domain to circumvent the detector bandwidth limit by using a swept-frequency optical waveform. Systems utilizing FMCW reflectometry, also known as swept-source optical coherence tomography (SS-OCT) in the biomedical optics community, are capable of resolutions of a few μm with low detection bandwidths. Moreover, optical FMCW is an interferometric technique in which the measured signal is proportional to the reflected electric field, as opposed to the reflected intensity, as in the TOF case. The signal levels due to a scatterer with reflectivity $R < 1$ are therefore proportional to R and $\sqrt{R}$ in TOF and FMCW systems, respectively. The combination of higher signal levels due to electric field dependence, and lower noise due to low detection bandwidths results in a significantly higher dynamic range and sensitivity of the FMCW system versus a TOF implementation [37,38]. As a result, FMCW reflectometry has found numerous applications, e.g., light detection and ranging (lidar) [18,19], biomedical imaging [20,21], non-contact profilometry [22,23] and biometrics [24,25].

2.1.1 Basic FMCW Analysis and Range Resolution

Let us first examine the problem of recovering single-scatterer depth information using a SFL. For simplicity, we consider a noiseless laser whose frequency changes linearly with time. The normalized electric field at the source, for a single chirp period, is given by

$$e(t) = \text{rect}\left(\frac{t - T/2}{T}\right)\cos\left(\phi_0 + \omega_0 t + \frac{\xi t^2}{2}\right), \tag{2.1}$$

where T is the scan duration, ξ is the slope of the optical chirp, and ϕ_0 and ω_0 are the initial phase and frequency, respectively. The rect function models the finite time-extent of the chirp and is defined by:

$$\text{rect}(x) \equiv \begin{cases} 0, & |x| > 1/2 \\ 1/2, & |x| = 1/2 \\ 1, & |x| < 1/2 \end{cases} \tag{2.2}$$

The instantaneous optical frequency is given by the time derivative of the argument of the cosine in equation (2.1)

$$\omega_{SFL}(t) = \frac{d}{dt}\left(\phi_0 + \omega_0 t + \frac{\xi t^2}{2}\right) = \omega_0 + \xi t \tag{2.3}$$

The total frequency excursion of the source (in Hz) is then given by $B = \xi T/2\pi$. We illuminate a single scatterer with the chirped field, and collect the reflected light. The time evolution of the frequencies of the launched and reflected beams is shown in figure 2.1. Because the chirp is precisely linear, a scatterer with a round-trip time delay τ (and a corresponding displacement $c\tau/2$ from the source) results in constant frequency difference $\xi\tau$ between the launched and reflected waves.

The FMCW technique relies on a measurement of this frequency differences to determine the time delay τ. This is accomplished in a straightforward way by recording the time-dependent interference signal between the launched and reflected waves on a photodetector. An FMCW measurement setup based on a Mach-Zehnder interferometer (MZI) is shown schematically in figure 2.2. Another common implementation
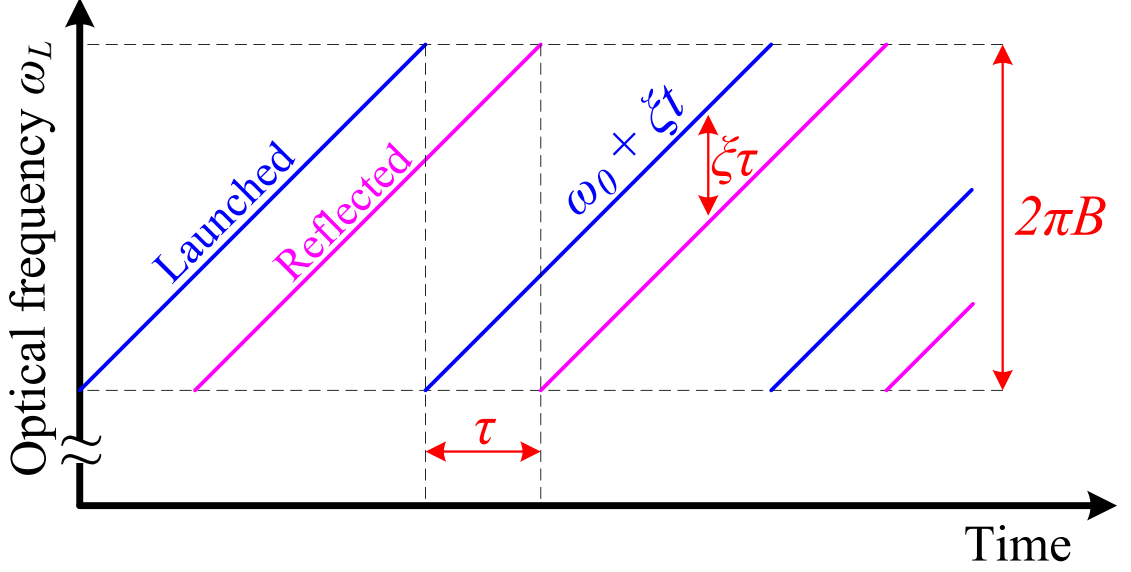
Figure 2.1: Time evolution of the optical frequencies of the launched and reflected waves in a single-scatterer FMCW ranging experiment

is based on a Michelson interferometer, and is shown in figure 2.3. In both implementations, the sum of the electric fields of the launched and reflected waves is incident on a photodetector. It is common to call the launched wave a local or a reference wave, and we will use all three terms interchangeably (hence the reference arm and reference mirror designations in the MZI and Michelson interferometer figures).

The normalized photocurrent is equal to the time-averaged intensity of the incident beam, and is given by

$$
\begin{aligned}
i(t) &= \left\langle \left| e(t) + \sqrt{R}\, e(t - \tau) \right|^2 \right\rangle_t \\
&= \operatorname{rect}\left(\frac{t - T/2}{T} \right) \left\{ \frac{1 + R}{2} + \sqrt{R} \cos\left[(\xi\tau)t + \omega_0\tau - \frac{\xi\tau^2}{2} \right] \right\},
\end{aligned}
\tag{2.4}
$$

where R is the target reflectivity, and we have assumed that $\tau << T$. The averaging, denoted by $\langle \cdot \rangle_t$, is done over an interval that is determined by the photodetector response time, and is much longer than an optical cycle, yet much shorter than the period of the cosine in equation (2.4). In the expressions that follow we drop the DC term $(1 + R)/2$ for simplicity. It is convenient to work in the optical frequency
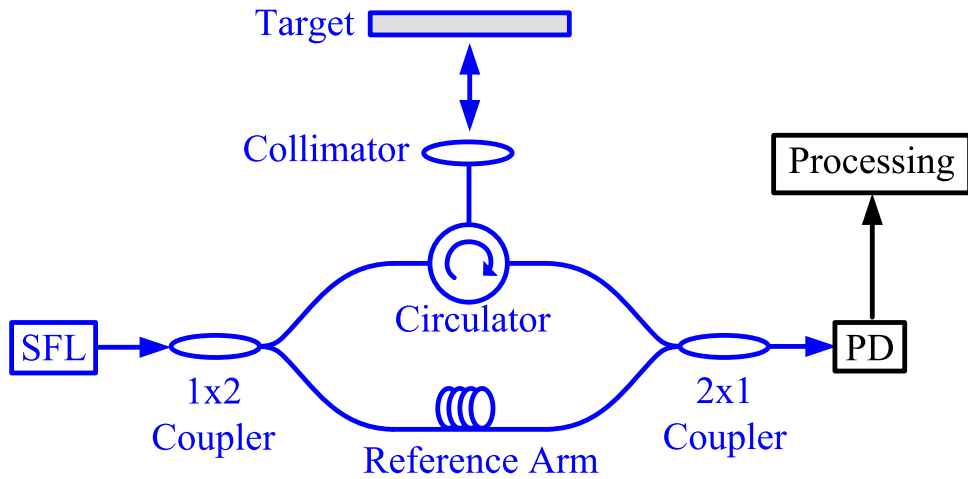
Figure 2.2: Mach-Zehnder interferometer implementation of the FMCW ranging experiment
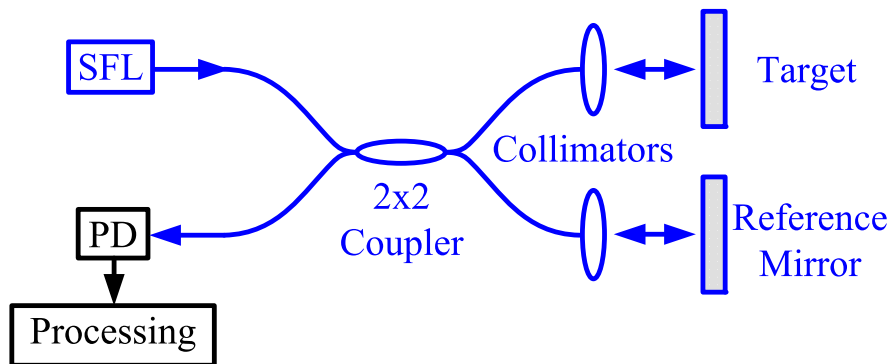

Figure 2.3: Michelson interferometer implementation of the FMCW ranging experiment

domain, so we use equation (2.3) to rewrite the photocurrent as a function of ω_{SFL}.

$$
\begin{aligned}
y(\omega_{SFL}) &\equiv i\left(\frac{\omega_{SFL} - \omega_0}{\xi}\right) \\
&= \sqrt{R}\,\text{rect}\left(\frac{\omega_{SFL} - \omega_0 - \pi B}{2\pi B}\right)\cos\left(\omega_{SFL}\tau - \frac{\xi\tau^2}{2}\right).
\end{aligned}
\tag{2.5}
$$

The delay τ is found by taking the Fourier transform (FT) of $y(\omega_{SFL})$ with respect to the variable ω_{SFL}, which yields a single sinc function centered at the delay τ.

$$
Y(\zeta) \equiv \mathcal{F}_{\omega_{SFL}}\{y(\omega_{SFL})\} = \pi B\sqrt{R}\,\exp\left(-j\frac{\xi\tau^2}{2}\right)\exp\left[-j(\zeta - \tau)(\omega_0 + \pi B)\right]\text{sinc}\left[\pi B(\zeta - \tau)\right],
\tag{2.6}
$$

where ζ is the independent variable of the FT of $y(\omega_{SFL})$, and has units of time, and $\text{sinc}(x) = \frac{\sin x}{x}$. Additionally, we only consider positive Fourier frequencies since the signals of interest are purely real, and the FT therefore possesses symmetry about $\zeta = 0$.

A collection of scatterers along the direction of beam propagation arising, for example, from multiple tissue layers in an SS-OCT application, results in a collection of sinusoidal terms in the photodetector current, so that equation (2.6) becomes:

$$
Y(\zeta) = \pi B\sum_n \sqrt{R_n}\,\exp\left(-j\frac{\xi\tau_n^2}{2}\right)\exp\left[-j(\zeta - \tau_n)(\omega_0 + \pi B)\right]\text{sinc}\left[\pi B(\zeta - \tau_n)\right],
\tag{2.7}
$$

where τ_n and R_n are the round-trip time delay and the reflectivity of the n-th scatterer. Each scatterer manifests itself as a sinc function positioned at its delay, with a strength determined by its reflectivity. The ζ-domain description is therefore a map of scatterers along the axial direction.

The range resolution is traditionally chosen to correspond to the coordinate of the first null of the sinc function in equation (2.6) [39]. The null occurs at $\zeta = \tau + 1/B$, which corresponds to a free-space axial resolution

$$
\Delta z = \frac{c}{2B}.
\tag{2.8}
$$

The first constraint on the SFL is therefore the chirp bandwidth B—a large optical frequency range is necessary in order to construct a high-resolution imaging system. SS-OCT applications require resolutions below 10 μm in order to resolve tissue structure, and therefore make use of sources with bandwidths exceeding 10 THz.

An additional constraint on the imaging system is the need for precise knowledge of the instantaneous optical frequency as a function of time—it was used in transforming the photocurrent to the ω-domain. In the preceding analysis we have assumed a linear frequency sweep. While chirp linearity is preferred since it simplifies signal processing, it is not strictly necessary. As long as $\omega_{SFL}(t)$ is known precisely, it is still possible to transform the measured signal to the optical frequency domain, and extract the scatterer depth information. Because most SFLs have nonlinear chirps, it is common practice to measure the instantaneous chirp rate in parallel with the measurement using a reference interferometer. A related technique relies on what is called a k-clock—an interferometer that is used to trigger photocurrent sampling at time intervals that correspond to equal steps in optical frequency [20]. The k-clock is therefore a hardware realization of the ω-domain transformation.

While nonlinear chirps can be dealt with, they require faster electronics in order to acquire the higher frequency photocurrents associated with a nonuniform chirp rate. The optoelectronic SFL described in chapter 3 uses active feedback to enable precise control of the instantaneous optical frequency. As a result, the chirp can be programmed to be exactly linear in advance, allowing the use of a lower detection bandwidth, and hence decreasing electronic noise in an FMCW measurement.

2.1.2 Balanced Detection and RIN

In the preceding FMCW analysis we have simplified the expressions by intentionally leaving out DC contributions to the photocurrent. This simplification, while valid in an ideal noiseless laser, needs further justification in a practical measurement. The output intensity of laser systems varies due to external causes such as temperature and acoustic fluctuations, and also due to spontaneous emission into the lasing mode [40].

These intensity fluctuations scale with the nominal output intensity and are termed relative intensity noise (RIN). In a laser with RIN, the terms which give rise to the DC components of equation (2.4), also give rise to a noise component that we call $n(t)$. Equation (2.4) is therefore modified to

$$i(t) = \text{rect}\left(\frac{t - T/2}{T}\right)\left\{\left(\frac{1+R}{2} + n(t)\right) + \sqrt{R}\cos\left[(\xi\tau)t + \omega_0\tau - \frac{\xi\tau^2}{2}\right]\right\}. \quad (2.9)$$

The term $n(t)$ is a random variable whose statistics depend on the environmental conditions, the type of laser used in the measurement, and on the frequency response of the detection circuit. While the DC terms are readily filtered out, $n(t)$ is broadband and can corrupt the signal. This corruption is particularly important when the scatterers are weak and the signal level is low.

Balanced detection is a standard way to null the contribution of the DC terms and RIN. It relies on the use of a 2x2 coupler and a pair of photodetectors to measure the intensities of both the sum and the difference of the reference and reflected electric fields. Mach-Zehnder interferometer (MZI) and Michelson interferometer balanced FMCW implementations are shown in figure 2.4 and figure 2.5. These measurements produce pairs of photocurrents

$$i_{\pm}(t) = \text{rect}\left(\frac{t - T/2}{T}\right)\left\{\left(\frac{1+R}{2} + n(t)\right) \pm \sqrt{R}\cos\left[(\xi\tau)t + \omega_0\tau - \frac{\xi\tau^2}{2}\right]\right\}. \quad (2.10)$$

Balanced processing consists of averaging the two photocurrents, yielding

$$i_{\text{diff}}(t) \equiv \frac{i_+(t) - i_-(t)}{2} = \text{rect}\left(\frac{t - T/2}{T}\right)\sqrt{R}\cos\left[(\xi\tau)t + \omega_0\tau - \frac{\xi\tau^2}{2}\right]. \quad (2.11)$$

The DC and RIN terms are nulled in the subtraction, justifying the simplification made earlier. However, small gain differences in the photodetector circuitry, as well as slight asymmetries in the splitting ratio of the 2x2 coupler, result in a small amount of residual DC and RIN being present in the balanced photocurrent. This places a further constraint on the SFL—it is desirable that the laser possess a minimal amount of RIN so as to limit the amount of noise left over after balancing, and therefore
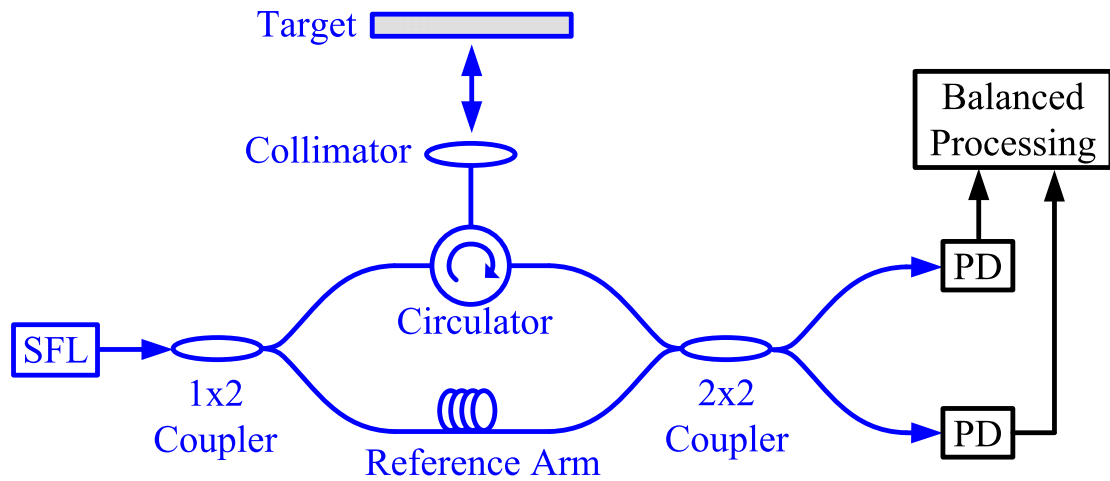
Figure 2.4: A balanced Mach-Zehnder interferometer implementation of the FMCW ranging experiment
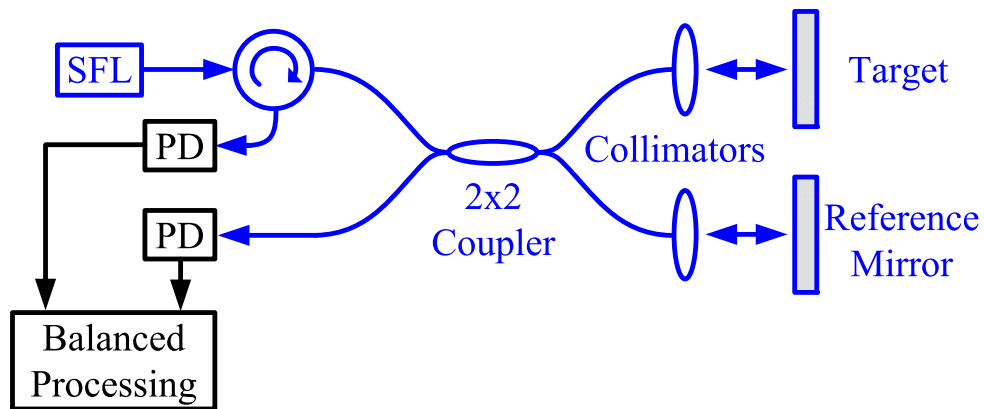

Figure 2.5: A balanced Michelson interferometer implementation of the FMCW ranging experiment

enhance the measurement dynamic range.

2.1.3 Effects of Phase Noise on the FMCW Measurement

So far we have assumed an SFL with a perfectly sinusoidal electric field. Practical lasers, however, exhibit phase and frequency noise. These fluctuations arise due to both external causes, such as thermal fluctuations, as well as due to spontaneous emission into the lasing mode [40]. These phenomena are responsible for a broadening of the spectrum of the electric field of a laser. In this section we analyze the effects of phase noise on the FMCW measurement. We begin by deriving the linewidth $\Delta\omega$ of single-frequency emission with phase noise. We then modify the FMCW equations to account for phase noise, derive its effects on fringe visibility, and define the notion of coherence time. To further quantify the effects of phase noise, we calculate the FMCW photocurrent spectrum. It will turn out that phase noise degrades the signal-to-noise ratio (SNR) with increasing target delay, putting a limit on the maximum range that can be reliably measured. We conclude by deriving statistical properties of the measurement accuracy, which help quantify system performance in a single-scatterer application (for example, profilometry).

2.1.3.1 Statistics and Notation

We first review some useful statistical results and introduce notation. For a wide-sense stationary random process $x(t)$, we denote its autocorrelation function by $\mathcal{R}_x$:

$$\mathcal{R}_x(u) = \mathcal{E}\left[x(t)x(t-u)\right], \tag{2.12}$$

where $\mathcal{E}[\cdot]$ is the statistical expectation value. For an ergodic random process, the expectation can be replaced by an average over all time, giving:

$$\mathcal{R}_x(u) = \langle x(t)x(t-u)\rangle_t, \tag{2.13}$$

By the Wiener–Khinchin theorem, the power spectral density (PSD) $\mathcal{S}_x(\omega)$ and autocorrelation $\mathcal{R}_x(u)$ are FT pairs.

$$\mathcal{S}_x(\omega) = \mathcal{F}_u\left[\mathcal{R}_x(u)\right] = \int_{-\infty}^{\infty} \mathcal{R}_x(u)e^{-i\omega u}du, \tag{2.14}$$

where $\mathcal{F}_u\left[\cdot\right]$ is the Fourier transform with respect to the variable u. We denote the variance of $x(t)$ by σ_x^2. For an ergodic process, the variance may be calculated in the time domain:

$$\sigma_x^2 = \left\langle x(t)^2 \right\rangle_t - \left\langle x(t)\right\rangle_t^2. \tag{2.15}$$

Alternatively, it may be calculated by integrating the PSD:

$$\sigma_x^2 = \frac{1}{2\pi}\int_{-\infty}^{\infty}\mathcal{S}_x(\omega)d\omega. \tag{2.16}$$

2.1.3.2   Linewidth of Single-Frequency Emission

We first derive a standard model for the spontaneous emission linewidth of a single-frequency laser [41]. The electric field is given by

$$e(t) = \cos\left[\omega_0 t + \phi_n(t)\right], \tag{2.17}$$

where $\phi_n(t)$ is a zero-mean stationary phase noise term. Plugging this expression into equation (2.13), we find the autocorrelation.

$$\mathcal{R}_e(u) = \left\langle \cos\left[\omega_0 t + \phi_n(t)\right]\cos\left[\omega_0(t-u) + \phi_n(t-u)\right]\right\rangle_t$$
$$= \frac{1}{2}\left\langle \cos\left[\omega_0 u + \Delta\phi_n(t,u)\right]\right\rangle_t + \frac{1}{2}\left\langle \cos\left[2\omega_0 t - \omega_0 u + \phi_n(t) + \phi_n(t-u)\right]\right\rangle_t, \tag{2.18}$$

where the sum term is crossed out because it averages out to zero. $\Delta\phi_n(t,u)$ is the accumulated phase error during time u, defined by

$$\Delta\phi_n(t,u) \equiv \phi_n(t) - \phi_n(t-u), \tag{2.19}$$

and is the result of a large number of independent spontaneous emission events. By the central limit theorem, $\Delta\phi_n(t, u)$ must be a zero-mean Gaussian random variable. The following identities therefore apply:

$$\langle \cos\left[\Delta\phi_n(t,u)\right]\rangle_t = \exp\left[-\frac{\sigma^2_{\Delta\phi_n}(u)}{2}\right], \text{ and } \langle \sin\left[\Delta\phi_n(t,u)\right]\rangle_t = 0. \tag{2.20}$$

So, equation (2.18) simplifies to

$$\mathcal{R}_e(u) = \frac{1}{2}\cos(\omega_0 u)\exp\left[-\frac{\sigma^2_{\Delta\phi_n}(u)}{2}\right]. \tag{2.21}$$

Taking the FT of equation (2.21), we find the spectrum of the electric field,

$$\mathcal{S}_e(\omega) = \frac{1}{4}\left[S_e^\circ(\omega - \omega_0) + S_e^\circ(\omega + \omega_0)\right], \tag{2.22}$$

where $S_e^\circ(\omega)$ is the baseband spectrum given by

$$S_e^\circ(\omega) = \mathcal{F}_u\left\{\exp\left[-\frac{\sigma^2_{\Delta\phi_n}(u)}{2}\right]\right\}. \tag{2.23}$$

To determine the emission lineshape we first consider the variance of the accumulated phase error. We start by expressing the autocorrelation of $\Delta\phi_n(t, u)$ in terms of the autocorrelation of $\phi_n(t)$. Using equation (2.13) and equation (2.19),

$$\mathcal{R}_{\Delta\phi_n}(s, u) = \langle \Delta\phi_n(t,u)\Delta\phi_n(t-s,u)\rangle_t = 2\mathcal{R}_{\phi_n}(s) - \mathcal{R}_{\phi_n}(s+u) - \mathcal{R}_{\phi_n}(s-u). \tag{2.24}$$

The PSD is given by

$$\begin{aligned}
\mathcal{S}_{\Delta\phi_n}(\omega, u) = \mathcal{F}_s\left[\mathcal{R}_{\Delta\phi_n}(s, u)\right] &= \mathcal{S}_{\phi_n}(\omega)\left(2 + e^{j\omega u} + e^{-j\omega u}\right) \\
&= 4\mathcal{S}_{\phi_n}(\omega)\sin^2(\omega u) = 4u^2\mathcal{S}_{\dot\phi_n}(\omega)\text{sinc}^2(\omega u),
\end{aligned} \tag{2.25}$$

where $\mathcal{S}_{\dot\phi_n}(\omega) = \omega^2\mathcal{S}_{\phi_n}(\omega)$ is the spectrum of the frequency noise $\dot\phi_n$. Spontaneous emission into the lasing mode gives rise to a flat frequency noise spectrum [40, 42],

and we therefore assign a constant value to $\mathcal{S}_{\dot{\phi}_n}(\omega)$,

$$\mathcal{S}_{\dot{\phi}_n}(\omega) \equiv \Delta\omega. \tag{2.26}$$

We plug equation (2.25) and equation (2.26) into equation (2.16) to calculate the variance of the accumulated phase error.

$$
\begin{aligned}
\sigma^2_{\Delta\phi_n}(u) &= \frac{1}{2\pi}\int_{-\infty}^{\infty}\mathcal{S}_{\Delta\phi_n}(\omega,u)d\omega \\
&= \frac{1}{2\pi}\int_{-\infty}^{\infty}4u^2\Delta\omega\ \mathrm{sinc}^2(\omega u)d\omega \\
&= |u|\Delta\omega.
\end{aligned}
\tag{2.27}
$$

Plugging this result into equation (2.23), we obtain the baseband spectrum of the electric field.

$$
\begin{aligned}
S_e^{\circ}(\omega) &= \mathcal{F}_u\left\{\exp\left[-\frac{\sigma^2_{\Delta\phi_n}(u)}{2}\right]\right\} = \mathcal{F}_u\left[\exp\left(-|u|\frac{\Delta\omega}{2}\right)\right] \\
&= \frac{\Delta\omega}{(\Delta\omega/2)^2 + \omega^2}.
\end{aligned}
\tag{2.28}
$$

The presence of phase noise broadens the baseband spectrum from a delta function to a Lorentzian function with a full width at half maximum (FWHM), or linewidth, of $\Delta\omega$.

To summarize, a flat frequency noise spectrum with a value of $\Delta\omega$ corresponds to a linewidth of $\Delta\omega$.

$$\mathcal{S}_{\dot{\phi}_n}(\omega) = \Delta\omega \iff \text{linewidth } \Delta\omega \text{ (rad/s)} \tag{2.29}$$

So far we have been using angular frequency units (rad/s) for both frequency noise and linewidth. Ordinary frequency units (Hz) are often used, so we convert the relation in equation (2.29) to

$$\mathcal{S}_{\frac{\dot{\phi}_n}{2\pi}}(\nu) = \frac{1}{(2\pi)^2}\mathcal{S}_{\dot{\phi}_n}(2\pi\nu) = \frac{\Delta\nu}{2\pi} \iff \text{linewidth } \Delta\nu = \frac{\Delta\omega}{2\pi} \text{ (Hz)}, \tag{2.30}$$

where $\nu = \omega/(2\pi)$ is the Fourier frequency in Hz. In practice, there are other noise sources that give rise to a $1/f$ behavior of the frequency noise spectrum. It has been shown that such noise sources generate a Gaussian lineshape [43].

As an exercise, we numerically verify equation (2.30) using a Monte Carlo simulation. We model a flat angular frequency noise spectrum by drawing samples from a zero-mean Gaussian distribution. These frequency noise samples are integrated in time, and the cosine of the resultant phase noise is calculated. The PSD of this signal therefore corresponds to half the baseband spectrum of equation (2.28). Each iteration of this procedure is performed over a finite time T, and therefore yields only an *estimate* of the true PSD. If the angular frequency resolution $2\pi/T$ is much smaller than the angular linewidth $\Delta\omega$, the mean of this estimate, over many iterations, will converge to equation (2.28) [44].

Estimates of baseband electric field spectra corresponding to $\mathcal{S}_{\dot{\phi}_n}(\omega) = 2\pi(1 \text{ MHz})$ are shown in blue in figure 2.6. As the number of iterations N used in the calculation is increased, the simulated PSD converges to the true PSD of equation (2.28), shown in red. Simulated frequency noise spectra and corresponding baseband lineshapes for three different values of $\Delta\omega$ are plotted in figure 2.7, illustrating the relation of equation (2.29).

2.1.3.3 Fringe Visibility in an FMCW Measurement

We continue or analysis by modifying the chirped electric field in equation (2.1) to include phase noise,

$$e(t) = \text{rect}\left(\frac{t - T/2}{T}\right)\cos\left(\phi_0 + \omega_0 t + \frac{\xi t^2}{2} + \phi_n(t)\right), \qquad (2.31)$$

and assume a perfect reflector ($R = 1$). The photocurrent is therefore given by

$$i(t) = \text{rect}\left(\frac{t - T/2}{T}\right)\left\{1 + \cos\left[(\xi\tau)t + \omega_0\tau - \frac{\xi\tau^2}{2} + \Delta\phi_n(t,\tau)\right]\right\}, \qquad (2.32)$$
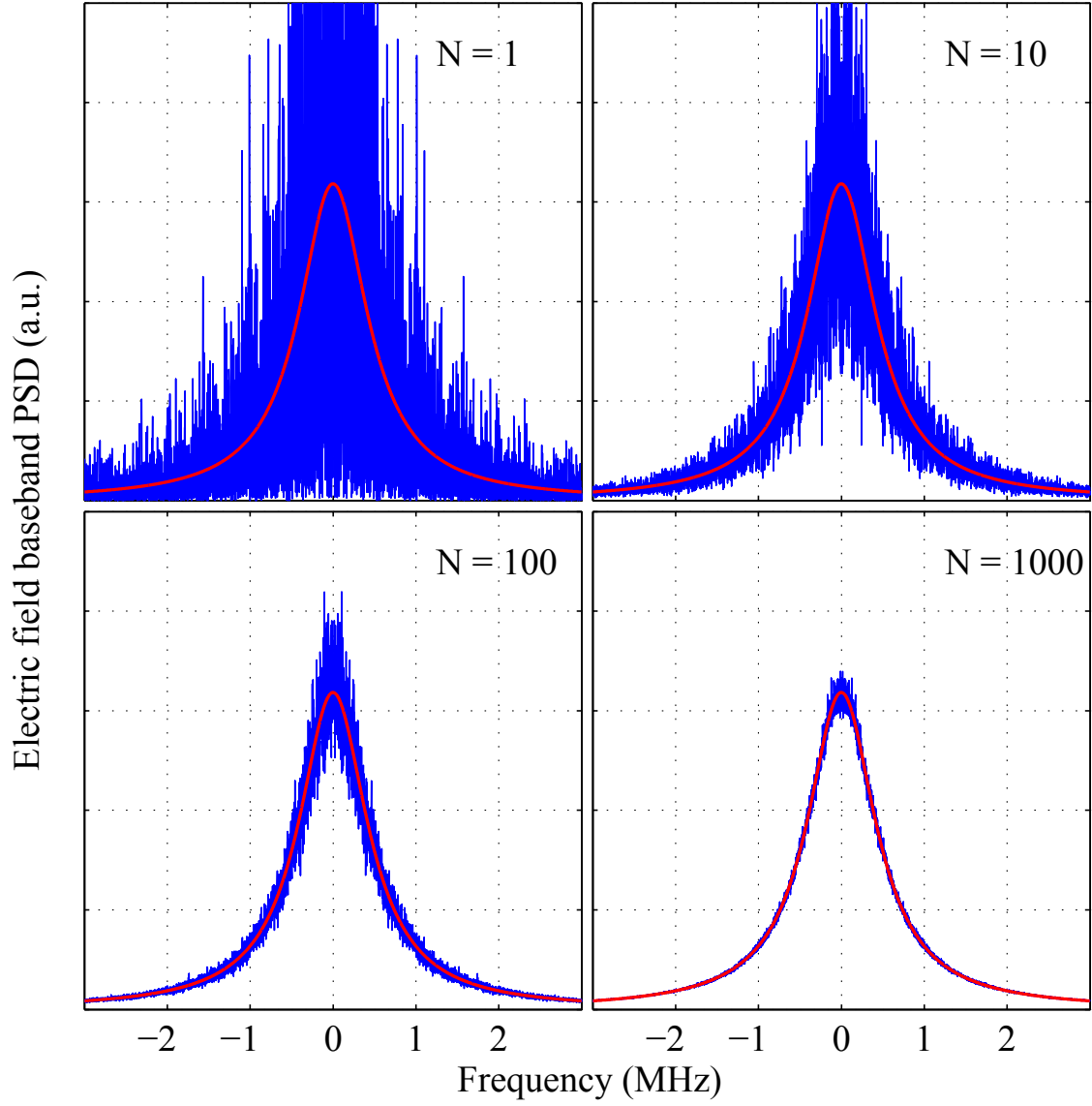
Figure 2.6: Convergence of the Monte Carlo simulation of the baseband electric field spectrum (blue) to the theoretical expression (red). The angular linewidth is $\Delta\omega = 2\pi(1\ \text{MHz})$. N is the number of iterations used in calculating the PSD estimate.
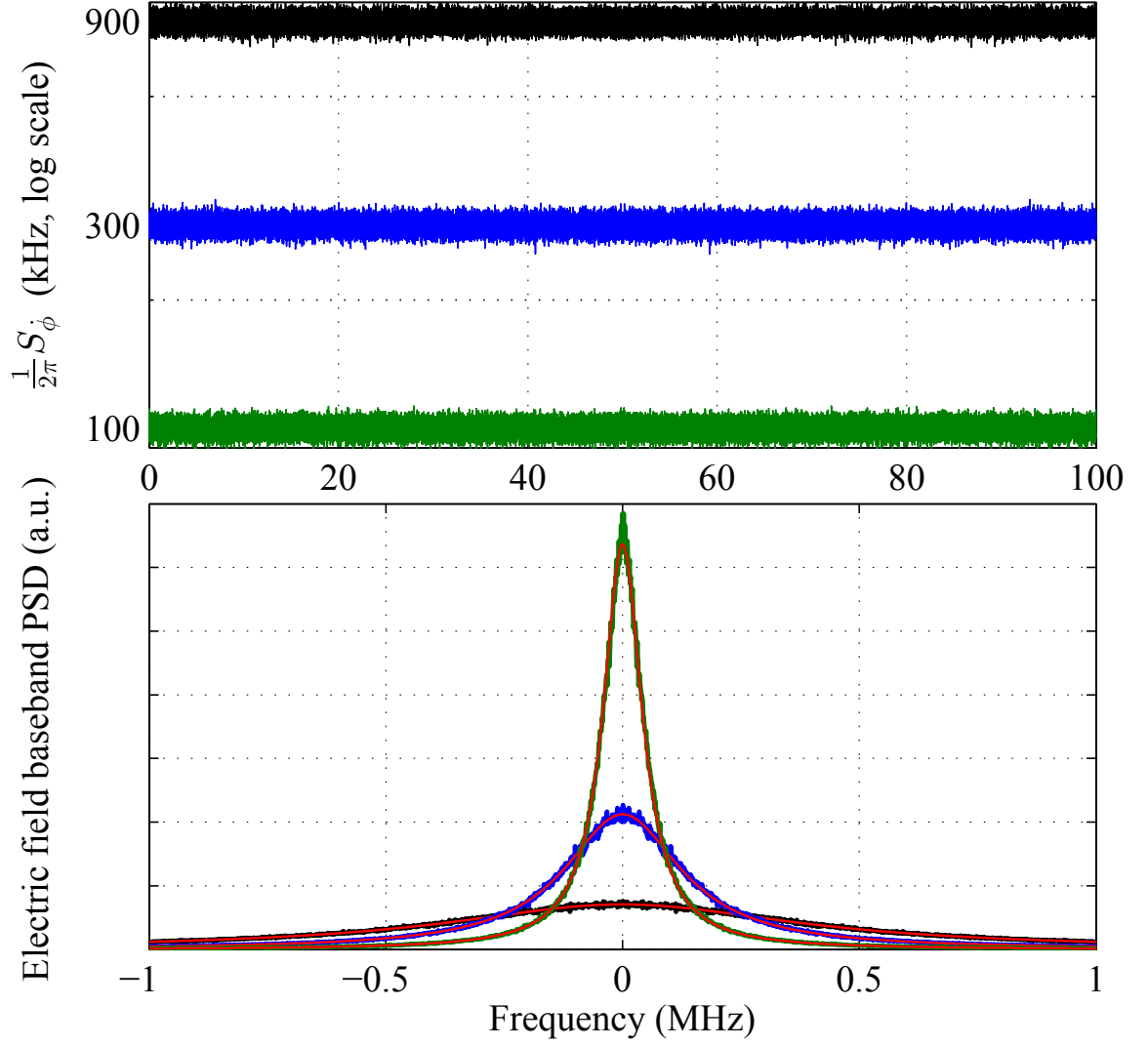
Figure 2.7: Normalized frequency noise spectra (top panel) and corresponding base-band electric field spectra (bottom panel) for $\Delta\omega = 2\pi(900\,\text{kHz})$ (black), $2\pi(300\,\text{kHz})$ (blue), and $2\pi(100\,\text{kHz})$ (green). The spectra are averaged over N=1000 iterations. The red curves are plots of the theoretical lineshape for the three values of $\Delta\omega$.

where $\Delta\phi_n(t,\tau)$ is the familiar accumulated phase error during time τ. In the noiseless case, the oscillations (fringes) in the photocurrent extend from 0 to 2. The presence of phase noise will add jitter to the locations of the peaks and troughs. The amplitude of the fringes, averaged over many scans, is therefore expected to decrease with increasing phase noise. To quantify this effect, we define the fringe visibility

$$V \equiv \frac{i_{max} - i_{min}}{i_{max} + i_{min}}, \tag{2.33}$$

where i_{max} and i_{min} are the photocurrent values at the peaks and troughs, averaged over many scans. The visibility takes on a value of 1 in the noiseless case, and goes to zero as the amount of noise increases. Using the identities in equation (2.20), we write down expressions for the maximum and minimum currents,

$$\begin{aligned} i_{max} &= 1 + \exp\left[-\frac{\sigma^2_{\Delta\phi_n}(\tau)}{2}\right], \text{ and} \\ i_{min} &= 1 - \exp\left[-\frac{\sigma^2_{\Delta\phi_n}(\tau)}{2}\right]. \end{aligned} \tag{2.34}$$

Plugging in equation (2.27) and equation (2.34) into equation (2.33), we arrive at an expression for the phase-noise-limited visibility [45],

$$V = \exp\left(-|\tau|\frac{\Delta\omega}{2}\right) = \exp\left(-\frac{|\tau|}{\tau_c}\right), \tag{2.35}$$

where

$$\tau_c \equiv \frac{2}{\Delta\omega} = \frac{1}{\pi\Delta\nu} \tag{2.36}$$

is the coherence time of the SFL. For delays much shorter than the coherence time, the visibility decreases linearly with τ. Once τ is comparable to τ_c, the visibility drops exponentially. The coherence time is therefore a measure of the longest range that can be acquired by an FMCW system.

2.1.3.4 Spectrum of the FMCW Photocurrent and the SNR

The signal-to-noise ratio (SNR) is more useful in quantifying the effect of phase noise than the visibility. To determine the SNR we must first calculate the photocurrent spectrum. We assume a balanced detector and disregard, for now, the rect function that models the finite chirp bandwidth of the SFL. The photocurrent expression becomes

$$i(t) = \sqrt{R} \cos\left[(\xi\tau)t + \omega_0\tau - \frac{\xi\tau^2}{2} + \Delta\phi_n(t, \tau)\right]. \tag{2.37}$$

Plugging this expression into equation (2.13), we find the autocorrelation,

$$
\begin{aligned}
\mathcal{R}_i(u) &= \frac{R}{2} \left\langle \cos\left[(\xi\tau)u + \Delta\phi_n(t, \tau) - \Delta\phi_n(t - u, \tau)\right]\right\rangle_t \\
&= \frac{R}{2} \left\langle \cos\left[(\xi\tau)u + \theta(t, \tau, u)\right]\right\rangle_t \\
&= \frac{R}{2} \cos\left[(\xi\tau)u\right] \exp\left[-\frac{\sigma_\theta^2(\tau, u)}{2}\right],
\end{aligned}
\tag{2.38}
$$

where

$$\theta(t, \tau, u) \equiv \Delta\phi_n(t, \tau) - \Delta\phi_n(t - u, \tau), \tag{2.39}$$

and we have assumed that $\theta(t, \tau, u)$ possesses Gaussian statistics. Taking the FT of equation (2.38), we find the spectrum of the photocurrent.

$$\mathcal{S}_i(\omega) = \frac{1}{4}\left[S_i^\circ(\omega - \xi\tau) + S_i^\circ(\omega + \xi\tau)\right], \tag{2.40}$$

where $S_i^\circ(\omega)$ is the baseband spectrum given by

$$S_i^\circ(\omega) = \mathcal{F}_u\left\{\exp\left[-\frac{\sigma_{\theta(\tau,u)}^2}{2}\right]\right\}. \tag{2.41}$$

To find the baseband spectrum and the SNR we need to calculate the variance of $\theta(t, \tau, u)$. First we derive a useful identity. Let us write down the variance of $\Delta\phi_n(t, u)$,

as it is defined in equation (2.15),

$$\sigma^2_{\Delta\phi_n}(u) = \left\langle [\phi_n(t) - \phi_n(t - u)]^2 \right\rangle_t$$
$$= 2\sigma^2_{\phi_n} - 2\left\langle \phi_n(t)\phi_n(t - u) \right\rangle_t. \tag{2.42}$$

This gives us an expression for the autocorrelation of $\phi_n(t)$,

$$\mathcal{R}_\phi(u) = \left\langle \phi_n(t)\phi_n(t - u) \right\rangle_t = \sigma^2_{\phi_n} - \frac{\sigma^2_{\Delta\phi_n}(u)}{2}. \tag{2.43}$$

We plug this result into equation (2.24),

$$\mathcal{R}_{\Delta\phi_n}(s, u) = 2\mathcal{R}_{\phi_n}(s) - \mathcal{R}_{\phi_n}(s + u) - \mathcal{R}_{\phi_n}(s - u)$$
$$= \frac{\sigma^2_{\Delta\phi_n}(s + u)}{2} + \frac{\sigma^2_{\Delta\phi_n}(s - u)}{2} - \sigma^2_{\Delta\phi_n}(s). \tag{2.44}$$

We are now in a position to calculate the variance of $\theta(t, \tau, u)$. Beginning with the definition in equation (2.15),

$$\sigma^2_\theta(\tau, u) = \left\langle [\Delta\phi_n(t, \tau) - \Delta\phi_n(t - u, \tau)]^2 \right\rangle_t$$
$$= \left\langle \Delta\phi_n(t, \tau)^2 + \Delta\phi_n(t - u, \tau)^2 - 2\Delta\phi_n(t, \tau)\Delta\phi_n(t - u, \tau) \right\rangle_t \tag{2.45}$$
$$= 2\sigma^2_{\Delta\phi_n}(\tau) - 2\mathcal{R}_{\Delta\phi_n}(u, \tau).$$

Plugging in equation (2.44), we arrive at

$$\sigma^2_\theta(\tau, u) = 2\sigma^2_{\Delta\phi_n}(\tau) + 2\sigma^2_{\Delta\phi_n}(u) - \sigma^2_{\Delta\phi_n}(u + \tau) - \sigma^2_{\Delta\phi_n}(u - \tau). \tag{2.46}$$

Using the result of equation (2.27), we write down a final expression for the variance of $\theta(t, \tau, u)$,

$$\sigma^2_\theta(\tau, u) = \Delta\omega \left(2\tau + 2|u| - |u - \tau| - |u + \tau|\right)$$
$$= \begin{cases} \dfrac{4|u|}{\tau_c} & |u| \leq \tau, \\ \dfrac{4\tau}{\tau_c} & |u| > \tau. \end{cases} \tag{2.47}$$

The baseband photocurrent spectrum is found by plugging equation (2.47) into equation (2.41), yielding [46, 47]

$$
\begin{aligned}
S_i^\circ(\omega) &= \mathcal{F}_u\left\{\exp\left[-\frac{\sigma_{\theta(\tau,u)}^2}{2}\right]\right\} \\
&= 2\pi\delta(\omega)e^{-\frac{2\tau}{\tau_c}} + \frac{\tau_c}{1 + \left(\frac{\omega\tau_c}{2}\right)^2}\left\{1 - e^{-\frac{2\tau}{\tau_c}}\left[\cos(\omega\tau) + \frac{2}{\omega\tau_c}\sin(\omega\tau)\right]\right\}.
\end{aligned}
\tag{2.48}
$$

This expression has two terms—the delta function that represents the beat signal due to an interference of the reference and reflected beams, and the noise pedestal that arises as a result of the finite coherence time of the chirped beam. Each FMCW measurement is performed over a finite time T, and its PSD is therefore only an estimate of equation (2.48). The expected spectrum is given by the convolution of equation (2.48) and the PSD of the rect function that accompanies the electric field of equation (2.31) [44],

$$
\begin{aligned}
S_i^\circ(\omega, T) &= \frac{1}{2\pi}S_i^\circ(\omega) \star \left[T\mathrm{sinc}^2\left(\frac{\mathrm{T}\omega}{2}\right)\right] \\
&= T\mathrm{sinc}^2\left(\frac{\mathrm{T}\omega}{2}\right)e^{-\frac{2\tau}{\tau_c}} + \frac{\tau_c}{1 + \left(\frac{\omega\tau_c}{2}\right)^2}\left\{1 - e^{-\frac{2\tau}{\tau_c}}\left[\cos(\omega\tau) + \frac{2}{\omega\tau_c}\sin(\omega\tau)\right]\right\}.
\end{aligned}
\tag{2.49}
$$

In performing this convolution we have assumed that the scan time is the slowest time scale in the model, i.e., $T \gg \tau$ and $T \gg \tau_c$, so that the sinc-squared PSD of the rect function effectively acts as a delta function when convolved with the spectrum of the noise pedestal. Plots of equation (2.49) for four different values of τ/τ_c are shown in figure 2.8. The scan time is $T = 1$ ms and the coherence time is $\tau_c = 1$ μs. The spectra are normalized to the level of the noise at $\omega = 0$. In the coherent regime, i.e., $\tau \ll \tau_c$, the PSD comprises a sinc-squared signal peak and a broad noise pedestal with oscillations. The period of these oscillations is given by $2\pi/\tau$. As the delay is increased, the signal peak shrinks, and the noise pedestal grows, until we obtain a Lorentzian profile with a FWHM of $2\Delta\omega$. This is what we expect for a beat spectrum of two uncorrelated beams with a linewidth of $\Delta\omega$ each.
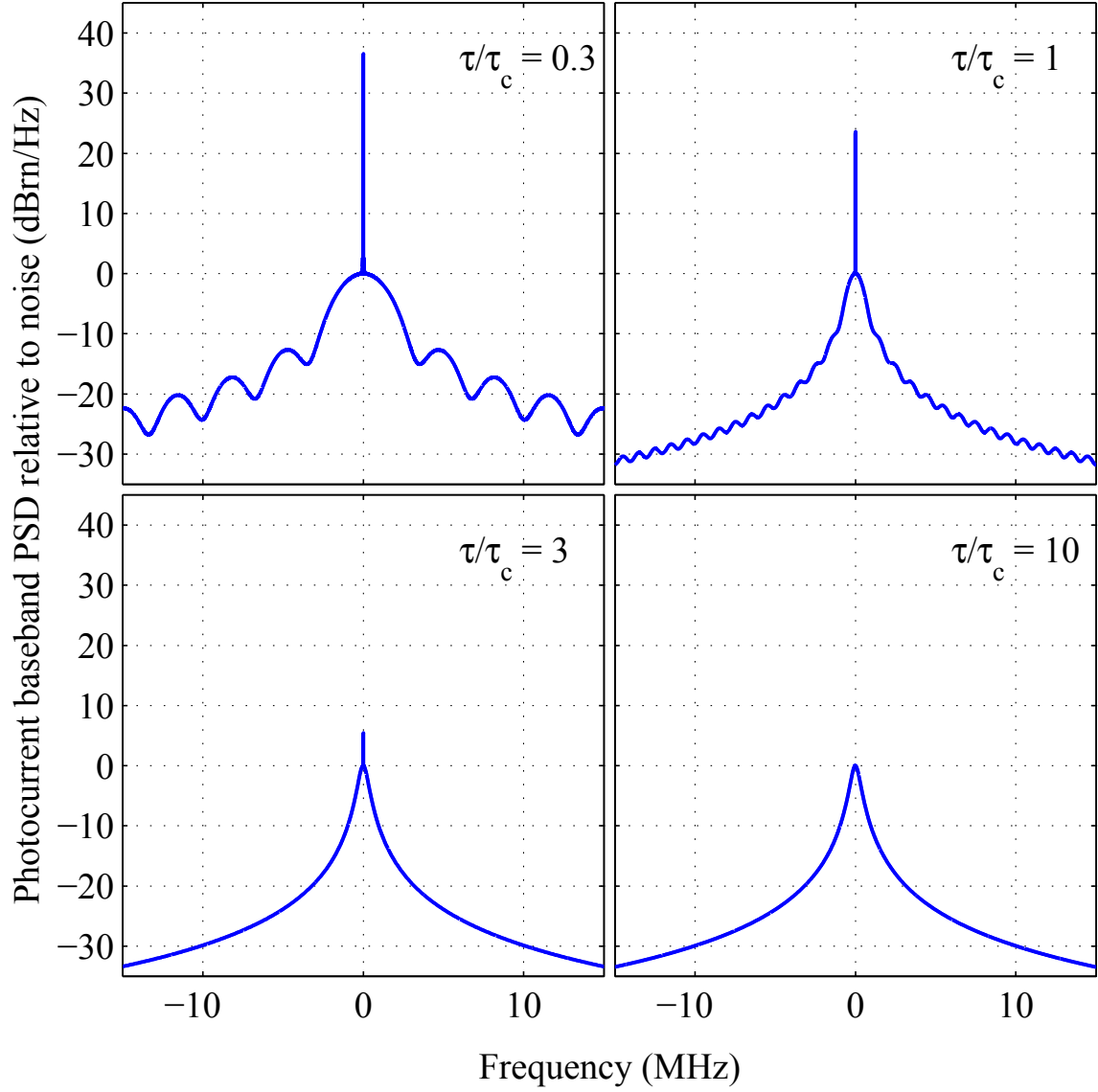
Figure 2.8: Baseband FMCW photocurrent spectra for four different values of τ/τ_c, normalized to zero-frequency noise levels. The scan time is $T = 1$ ms and the coherence time is $\tau_c = 1$ μs.
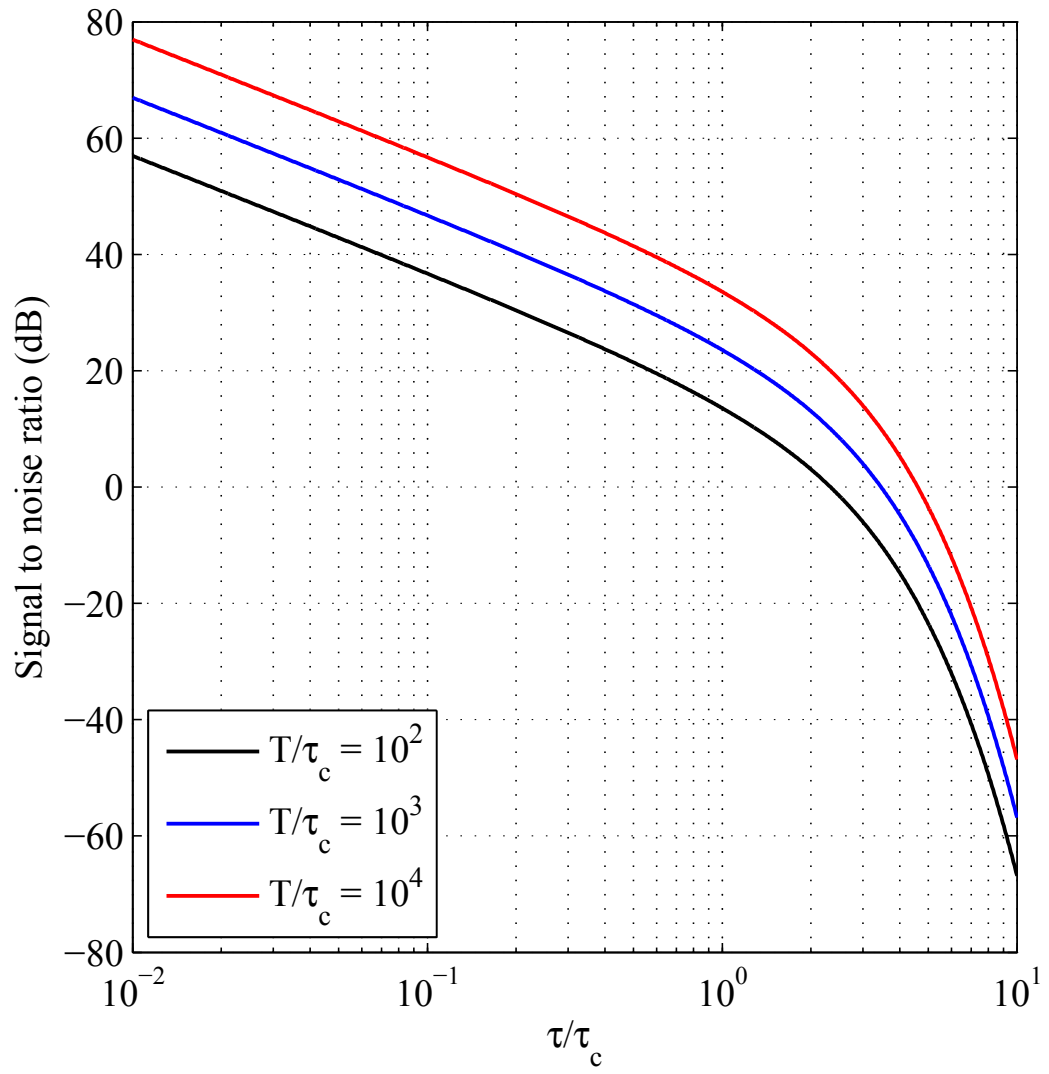
Figure 2.9: FMCW SNR as a function of τ/τ_c for three different values of T/τ_c

The SNR is readily calculated from equation (2.49), and is given in decibel units by

$$\text{SNR}_{\text{dB}} = 10 \log_{10} \left[\frac{T}{\tau_i} \times \frac{1}{e^{2\tau/\tau_c} - \left(1 + \frac{2\tau}{\tau_c}\right)} \right]. \tag{2.50}$$

A plot of the SNR versus τ/τ_c is shown in figure 2.9 for three different values of T/τ_c. In the coherent regime, the SNR decreases at 20 dB/decade with τ/τ_c, and drops sharply for $\tau > \tau_c$. This is consistent with the rapid decrease in visibility for delays longer than the coherence time, as predicted by equation (2.35). As the current analysis shows, the visibility is not the full story—even low fringe visibilities can result in a decent SNR, provided that the scan time T is long enough.

2.1.3.5 Phase-Noise-Limited Accuracy

The axial resolution of an FMCW system, $\Delta z = c/2B$, quantifies its ability to tell apart closely-spaced scatterers. If we assume that the beam only encounters a single scatterer, as it would in a profilometry application, then the relevant system metric is the accuracy—the deviation of the measured target delay τ^m from the true target delay τ. We briefly consider statistical properties of the accuracy using the phase noise model developed above.

The instantaneous photocurrent frequency in a single-scatterer FMCW experiment is given by a derivative of the cosine phase in equation (2.37),

$$\omega_{PD}(t) = \xi\tau + \frac{d}{dt}\Delta\phi_n(t, \tau). \tag{2.51}$$

The target delay is calculated from an average of the photocurrent frequency over the scan time T,

$$\xi\tau^m = \frac{1}{T} \int_0^T \omega_{PD}(t) = \xi\tau + \frac{\Delta\phi_n(T, \tau) - \Delta\phi_n(0, \tau)}{T}. \tag{2.52}$$

The accuracy is therefore given by

$$\delta\tau \equiv \tau^m - \tau = \frac{\Delta\phi_n(T,\tau) - \Delta\phi_n(0,\tau)}{B}. \tag{2.53}$$

The accuracy of a single measurement is a zero-mean random process with standard deviation

$$\sigma_{\delta\tau} = \frac{1}{B}\sqrt{\frac{4\tau}{\tau_c}}, \tag{2.54}$$

where we have used equation (2.39) and equation (2.47). Likewise, the depth accuracy δz is characterized by the standard deviation

$$\sigma_{\delta z} = \frac{c}{2B}\sqrt{\frac{4\tau}{\tau_c}} = \Delta z\sqrt{\frac{4\tau}{\tau_c}}. \tag{2.55}$$

Equation (2.55) shows that by operating in the sub-coherent regime, $\tau \ll \tau_c$, it is possible to measure spatial features on a scale that is much finer than the axial resolution. We come back to this idea in section 3.5.2, where we are able to record surface variations on a scale of a few tens of microns using an FMCW system with an axial resolution of 300 μm.

2.1.4 Summary

We have introduced the technique of optical frequency-modulated continuous-wave reflectometry and outlined its advantages over TOF ranging in 3-D imaging applications. We have derived the dependence of axial resolution on the chirp bandwidth and introduced balanced detection as a way to mitigate intensity noise. We have shown that SFL linewidth puts an upper limit on the target range, introduced system performance metrics, and derived the dependence of these metrics on the SFL coherence length, target delay, and scan time.

An ideal SFL will possess a narrow linewidth, linear frequency tuning, high chirp bandwidth, and a low RIN. The semiconductor laser (SCL)-based optoelectronic SFL attains these qualities without moving parts, and is studied in detail in chapter 3.